

Ferromagnetic Mn–Al–C L1₀ Formation by Electric Current Assisted Annealing

Fernando Maccari,* Alexander Zintler, Thomas Brede, Iliya A. Radulov, Konstantin P. Skokov, Leopoldo Molina-Luna, and Oliver Gutfleisch

The ferromagnetic Mn–Al–C τ -phase (L1₀ tetragonal structure) shows intrinsic potential to be developed as a permanent magnet; however, this phase is metastable and is easily decomposed to nonmagnetic stable phases, affecting negatively the magnetic properties. Giving the necessity to careful control of its synthesis, the use of a novel approach is investigated using electric current-assisted annealing to obtain pure τ -phase samples. The temperature and electrical resistance of the samples are monitored during annealing and it is shown that the change in resistance can be used to probe the phase transformation. Upon increase of electric current density, the required temperature for the ferromagnetic phase formation is reduced, reaching a maximum shift of 140 °C at 45 A mm⁻². Even though this noticeable shift is achieved, the magnetic properties are not affected showing coercivity of 0.13 T and magnetization of 90 Am² kg⁻¹, independently from the electric current density used during annealing. Microstructural investigation reveals the nucleation of the τ -phase at the grain boundaries of the parent ϵ -phase. In addition, the existence of twin boundaries upon nucleation and growth of the metastable phase for all evaluated annealing conditions is observed, resulting in similar extrinsic magnetic properties.

1. Introduction

The development of Mn–Al-based ferromagnetic compounds has re-emerged in the past years as potential rare-earth (RE) free permanent magnets.^[1–5] This interest comes as a response to the 2011 RE crisis, where the prices for these critical elements increased substantially, allied with the increase in demand for magnetic materials for different applications, including e-mobility, data storage, automation, and generators.^[6–8] The significance of Mn–Al alloys is justified since it combines relative high intrinsic magnetic properties with the use of noncritical and low-cost elements.^[1,2] These points make this material system an interesting as a “gap magnet”, meaning that it has potential to fill the magnetic performance gap between Sr- and/or Ba-hexaferrites (cheap and low performance) and RE-based permanent magnets (Sm–Co and Nd–Fe–B—expensive and high performance), which is only partially covered by the use of bonded RE-based magnets.^[2,4,9]


Mn–Al compounds own their intrinsic magnetic potential to the sole ferromagnetic τ -phase, which shows an ordered tetragonal structure (L1₀ type) with theoretical maximum energy product been reported to be around 100–120 kJ m⁻³.^[1,10] However, this phase is metastable and can be easily decomposed into the nonmagnetic and thermodynamic stable γ_2 and β -Mn phases.^[11,12] In general, the τ -phase is obtained from a solid-state transformation from the high-temperature ϵ -phase (hcp structure), that can be either realized using a controlled cooling from high temperature or by using isothermal annealing, at moderate temperatures (450–600 °C), from a rapidly quenched ϵ -phase precursor.^[13,14] The mechanism behind the phase transformation is attributed to a combination of diffusion-controlled massive type and a shear (displacive)-type transformations, being dependent on the parent microstructure, chemical composition, and annealing conditions.^[12,15–17]

Given the metastable nature of the ferromagnetic phase, the processing window needs to be rigorously taken into consideration to control and maximize the τ -phase fraction to optimize magnetic properties. With this aim, in addition to the thermal treatment, chemical composition can also be used to hinder phase decomposition, being carbon doping reportedly to be effective in this regard.^[1,18] In addition to these traditional metallurgical variables (chemical composition and annealing parameters),

F. Maccari, I. A. Radulov, K. P. Skokov, O. Gutfleisch
Institute of Materials Science, Functional Materials
Technische Universität Darmstadt
64287 Darmstadt, Germany
E-mail: fernando.maccari@tu-darmstadt.de

A. Zintler, L. Molina-Luna
Institute of Materials Science, Advanced Electron Microscopy
Technische Universität Darmstadt
64287 Darmstadt, Germany

T. Brede
Institute of Materials Physics
Georg-August-Universität Göttingen
37075 Göttingen, Germany

 The ORCID identification number(s) for the author(s) of this article can be found under <https://doi.org/10.1002/adem.202201805>.

© 2023 The Authors. Advanced Engineering Materials published by Wiley-VCH GmbH. This is an open access article under the terms of the Creative Commons Attribution-NonCommercial-NoDerivs License, which permits use and distribution in any medium, provided the original work is properly cited, the use is non-commercial and no modifications or adaptations are made.

DOI: 10.1002/adem.202201805

techniques using the effect of magnetic field and electric current/fields during processing, despite not being extensively explored, can be used as an additional degree of freedom to potentially tailor and manipulate phase formation and microstructure.^[19–23] The effect of in-magnetic-field heat treatment (applied magnetic field up to 15 T) has been reported to accelerate the τ -phase formation without influencing the magnetic properties.^[24] Similarly, in our previous work, we have demonstrated that electric field-assisted technique (spark plasma sintering—SPS) also accelerates the metastable phase formation but also its decomposition.^[25] However, in our work, we also found that the electric current was not flowing through the Mn–Al–C sample during the SPS annealing, inhibiting possible additional side effects of electric current related to solid-state transformation, including changes in both temperature and kinetics, which were observed for other material systems.^[23,26,27] Such possibilities can be advantageous to control the τ -phase formation and further avoid the undesired decomposition.

In this study, we investigate the $\varepsilon \rightarrow \tau$ transformation in Mn–Al–C alloy by electric current-assisted annealing. The role of electric current and the effect of electric current density on the phase formation are examined and discussed. In addition, we confirmed that in situ electric resistance measurement can be used as an effective tool to probe the phase formation and phase control during annealing. Analysis of the magnetic properties is correlated with phase evolution and microstructural investigation.

2. Results and Discussion

2.1. Temperature-Induced $\varepsilon \rightarrow \tau$ Phase Transition

The differential scanning calorimetry (DSC) analysis during heating of $\text{Mn}_{54}\text{Al}_{44}\text{C}_2$, in as-spun state, shows a single exothermic peak around 470 °C, **Figure 1**. This peak is related to the $\varepsilon \rightarrow \tau$ phase transition, in agreement with the values reported in literature for melt-spun ribbons.^[13,28]

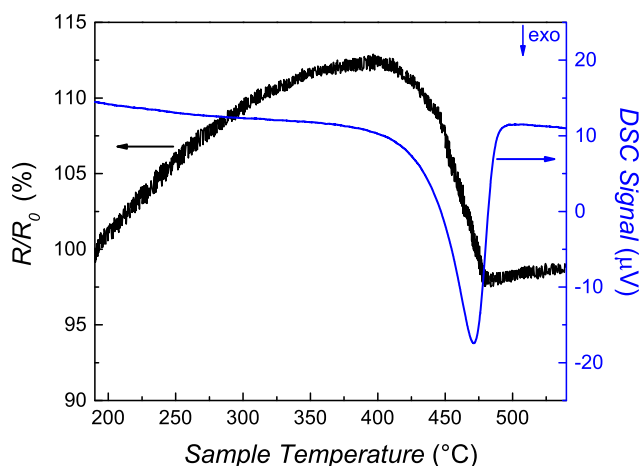


Figure 1. Differential scanning calorimetry (DSC) and electrical resistance variation in function of temperature showing $\varepsilon \rightarrow \tau$ phase transition in $\text{Mn}_{54}\text{Al}_{44}\text{C}_2$ melt-spun ribbons.

Comparatively to the DSC results, the relative electrical resistance variation (R/R_0) in function of the sample temperature using the in-house-built device is also shown in **Figure 1**. The R_0 value is defined as the initial electrical resistance while R is the resistance at the given sample temperature. The increment of the relative resistance value during heating up to 400 °C is related to the increase of sample temperature by the external heater (oven), leading to a higher scattering of the free electrons, resulting in higher electrical resistance, which is a typical feature for electric conductors.^[27] Increasing the sample temperature close to 420 °C, a decrease in the relative electrical resistance is observed, reaching a minimum value at 480 °C, followed by a plateau until the maximum temperature used in the analysis—550 °C. The change in the electrical resistance value within this temperature interval is related to the higher conductivity of the nucleated metastable τ -phase compared to the parent ε -phase. The difference in conductivity between both phases was reported by Rao,^[29] in agreement with the observed results, that is, higher electrical resistance of the parent ε -phase.

Comparing the results between the well-established DSC technique and the electrical resistance change, we note a good agreement on the temperature range for the phase transition in both analyses. Thus, it is possible to use the electrical resistance change as a tool to monitor phase transition between crystalline phases, even, as in this case, when a metastable phase is being formed. It is worth mentioning that the choice for using a relative low current density (2.5 A mm^{-2}), with negligible Joule heating, was to guarantee the similar conditions to the ones used in the DSC analysis.

2.2. Effect of Current Density on the $\varepsilon \rightarrow \tau$ Phase Transition

To study the possible effects of the electric current density on the phase-transition behavior, experiments varying the DC electric current density during annealing were performed. For this purpose, we evaluate the maximum electric current possible in terms of stability of the electronic signals (temperature and resistance) and also the mechanical integrity of the sample. It was found that for current densities above 45 A mm^{-2} the melt-spun ribbons were warping and, eventually, causing a mechanical failure, being the limiting factor for the experiment. Giving this constraint, current densities of 2.5, 15, 30, and 45 A mm^{-2} were selected for further experiments. It is worth mentioning that the electric current density was applied to the sample before putting the insert inside the oven. This methodology was used to record the sample temperature increase related to the Joule heating (ΔT_j) in the different conditions.

The relative electrical resistances in function of temperature for the different samples are shown in **Figure 2**. The annealing procedure was ceased after a drop in the relative electric resistance followed by a plateau, meaning that the transformation from the high-temperature phase to the metastable phase was completed, according to our previous observation shown in **Figure 1**. As the transition-temperature reference (T_τ), we take the 480 °C value as given similarly by both DSC and resistance change at low applied current density (2.5 A mm^{-2}), also shown in **Figure 2a**.

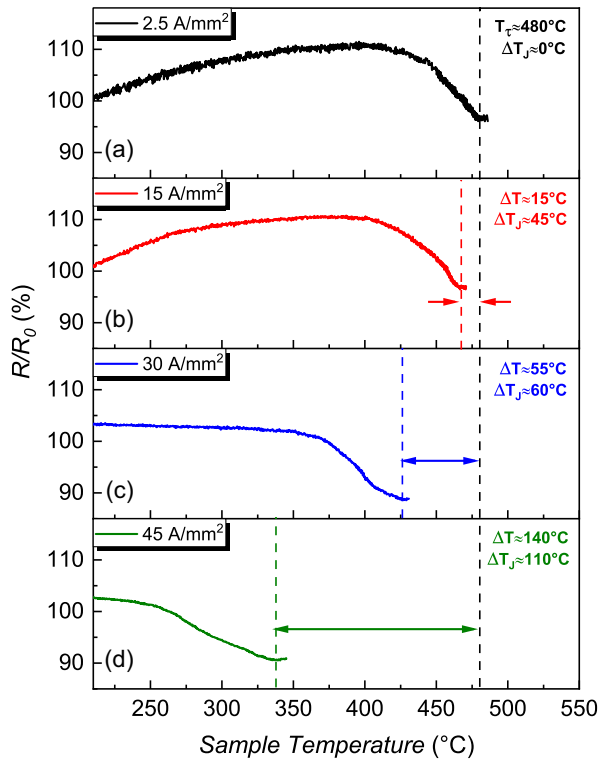


Figure 2. Electrical resistance in function of temperature for different electric current densities. The values of the rise in temperature cause by Joule heating (ΔT_J) and the temperature shift in the transition temperature (ΔT) are given.

One notices a gradual shift on the ϵ to τ transition (ΔT) toward lower temperatures with increasing the electric current density. The temperature shift using 15 A mm^{-2} during annealing is about 15°C (Figure 2b), while at 30 A mm^{-2} is 55°C (Figure 2c) and at 45 A mm^{-2} the ΔT reaches 140°C (Figure 2d). Similar trend was observed on the crystallization of amorphous metallic precursors.^[27,30] The change in the onset temperature can be associated to the possible formation of “hot spots,” meaning that structural and microstructural defects generate a higher resistance path for electric current causing a local overheating. The formation of these regions with higher temperature than the macroscopic temperature of the sample leads to a local changes of the atomic mobility and thermodynamic equilibrium, triggering nucleation of a stable or, as in this case, a metastable phase to emerge. It is worth mentioning that an increase of the macroscopic sample temperature, due to Joule heating (ΔT_J), was noticed and, as expected, the sample temperature increase is more pronounced at higher electric current densities, going from negligible values at 2.5 A mm^{-2} up to 110°C at 45 A mm^{-2} .

The phase transition from the hexagonal ϵ -phase to the tetragonal τ -phase was confirmed by X-ray diffraction (XRD) analysis (not shown). This indicates that the electric current-assisted annealing and the monitoring of the change in electrical resistance are feasible tools to obtain high pure ferromagnetic τ -phase samples and to circumvent the decomposition into the stable and nonmagnetic γ_2 and β -Mn phases.^[1,11,12]

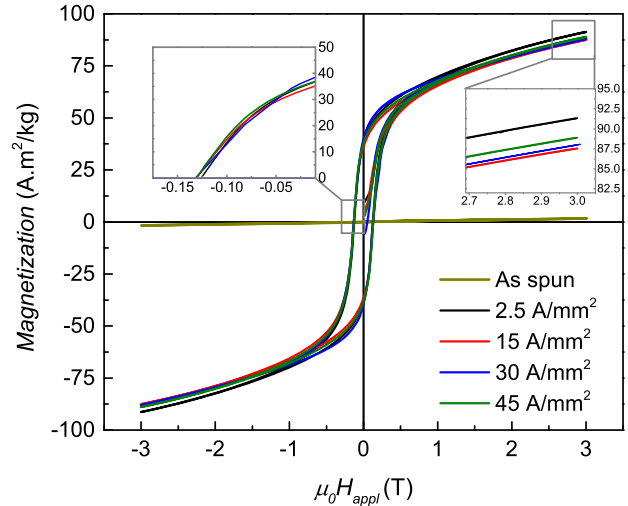


Figure 3. Isothermal magnetization measurements, at room temperature, of the samples annealed under different electric current densities in comparison to the as-spun state.

Moreover, isothermal magnetization measurements were performed to evaluate the impact of the electric current density during annealing on the magnetic properties. The hysteresis loops displayed in Figure 3 show a typical ferromagnetic response for the samples after annealing while paramagnetic in the as-spun state. The change of magnetic behavior reassures the phase transition from the paramagnetic high-temperature ϵ -phase to the ferromagnetic metastable τ -phase. Evaluating closely the magnetization value at 3 T (M_{3T}) applied magnetic field, almost no difference is seen between the samples, despite the current density used during annealing. The magnetization values lie in the range of $88\text{--}93 \text{ Am}^2 \text{ kg}^{-1}$, which are common values for pure τ -phase in Mn–Al–C compounds.^[18,25,31] Similarly, the coercivity values for all samples are within $0.12\text{--}0.14 \text{ T}$, which are typical reported values for conventionally annealed melt-spun ribbons.^[32,33] It is known that coercivity, being an extrinsic property, it is sensitive to microstructure and, specifically in Mn–Al compounds, it is often linked to the many possible defects resulting from the processing route and from the phase-transformation mechanism, as will be discussed in more detail in Section 2.3 focused on microstructural analysis.^[17,25,33–37]

2.3. Correlation of Change in Electrical Resistance and Phase Fraction

One important behavior observed during the phase transition is that the change in the relative electrical resistance is not abrupt, occurring in a temperature interval as shown previously in Figure 2. This opens the possibility to investigate the correlation between the phase formation and phase fraction with the variation in electrical resistance. For this purpose, experiments with fixed the electric current density were conducted and interrupted (quench) after different drops in the $\frac{\Delta R}{R_0}$ value.

Based on the previous experiment using electric current density at 30 A mm^{-2} , it is observed that the ϵ to τ -phase transition is

completed when the $\frac{\Delta R}{R_0}$ value drops by 15%, approximately. Taking this into consideration, the electric current density was kept fixed at 30 A mm^{-2} and the experiment was ceased when the $\frac{\Delta R}{R_0}$ value dropped 5% and 10%, approximately.

As can be seen in **Figure 4**, the three curves show similar trend and consistence (reproducible) regarding the transition temperature interval. As mentioned, the final data point in the curves mark the cease of the external heat and electric current supply.

To quantify the phase fraction, Rietveld analysis was performed on the XRD patterns shown in **Figure 5**. The calculated fraction of ϵ and τ are also given in Figure 5 in comparison to the initial sample state (as spun–pure ϵ -phase). The observed XRD patterns show the progression of ϵ to τ -phase transformation,

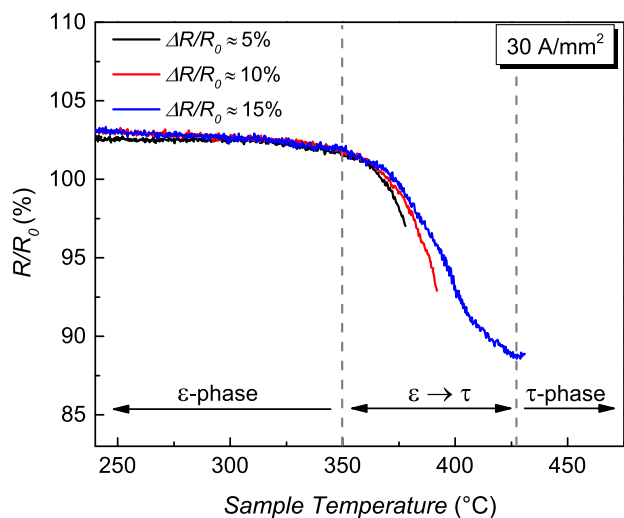


Figure 4. Electrical resistance variation in function of temperature of samples annealed under fixed electric current density of 30 A mm^{-2} and quenched at different states.

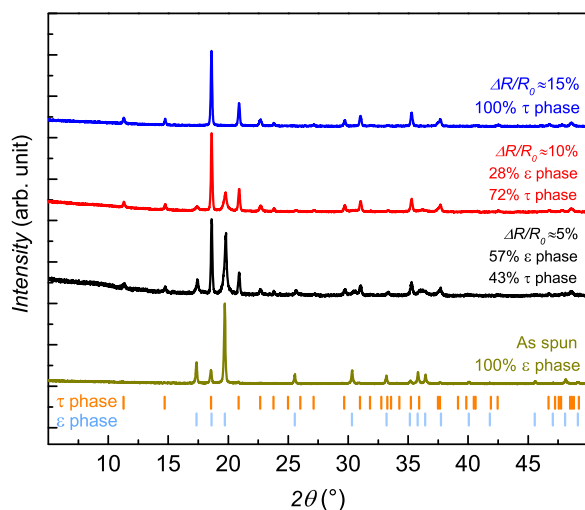


Figure 5. Diffraction patterns of the samples in the initial stage (as spun) and after different $\frac{\Delta R}{R_0}$ value drop during electric current–assisted annealing under a fixed current density of 30 A mm^{-2} .

with the relative intensity of the high-temperature hcp phase peaks decreasing until it completely vanishes and only peaks related to the tetragonal τ -phase are observed for the sample with $\frac{\Delta R}{R_0}$ decrease of 15%.

To further confirm these results and the impact on the functional properties, isothermal magnetization measurements were used to probe the ferromagnetic behavior of these samples, as shown in **Figure 6**. The magnetization value at 3 T (M_{3T}) is higher at higher drops in the $\frac{\Delta R}{R_0}$ value, from $40 \text{ Am}^2 \text{ kg}^{-1}$ for 5% to $88 \text{ Am}^2 \text{ kg}^{-1}$ for 15%. This rise in M_{3T} is directly related to the increase in the ferromagnetic phase fraction, coinciding to the XRD analysis. Interestingly, the coercivity value did not vary significantly between the samples, being independent on the phase fraction of the ferromagnetic phase and more related to the microstructure as aforementioned.

As confirmed from the XRD and magnetization measurements, the in situ measurements show good agreement between electrical resistance drop with the amount of τ -phase formed. This approach shows potential to be used as a tool to engineer microstructure and control phase fraction during annealing, including metastable phases.

2.4. Effect of Electric Current Density on the Microstructure

To gain more insight about the possible changes caused by electric current–assisted annealing and to correlate with the results from XRD and magnetic measurements, microstructural analysis was performed using transmission electron microscopy (TEM) in selected samples. We have chosen the partially transformed sample, under a fixed electric current density of 30 A mm^{-2} with $\frac{\Delta R}{R_0}$ decrease of 5%, that is, 43% of τ -phase and 57% of ϵ -phase, and the fully transformed samples (pure τ -phase) under the lowest and highest current density evaluated in this study (2.5 and 45 A mm^{-2}).

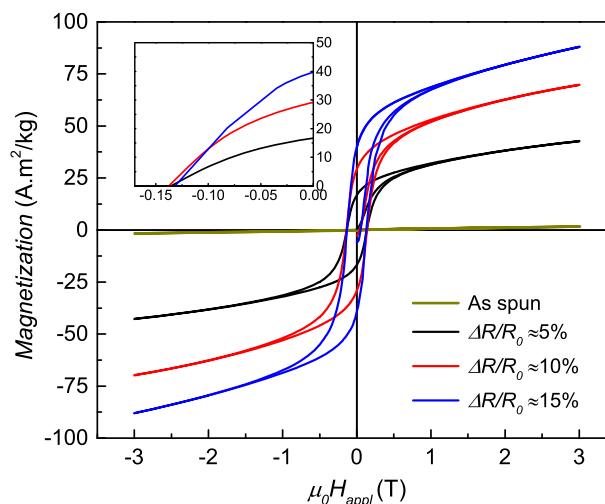


Figure 6. Isothermal magnetization measurements, at room temperature, of the samples in the initial stage (as spun) and after different $\frac{\Delta R}{R_0}$ values during electric current–assisted annealing with fixed current density of 30 A mm^{-2} .

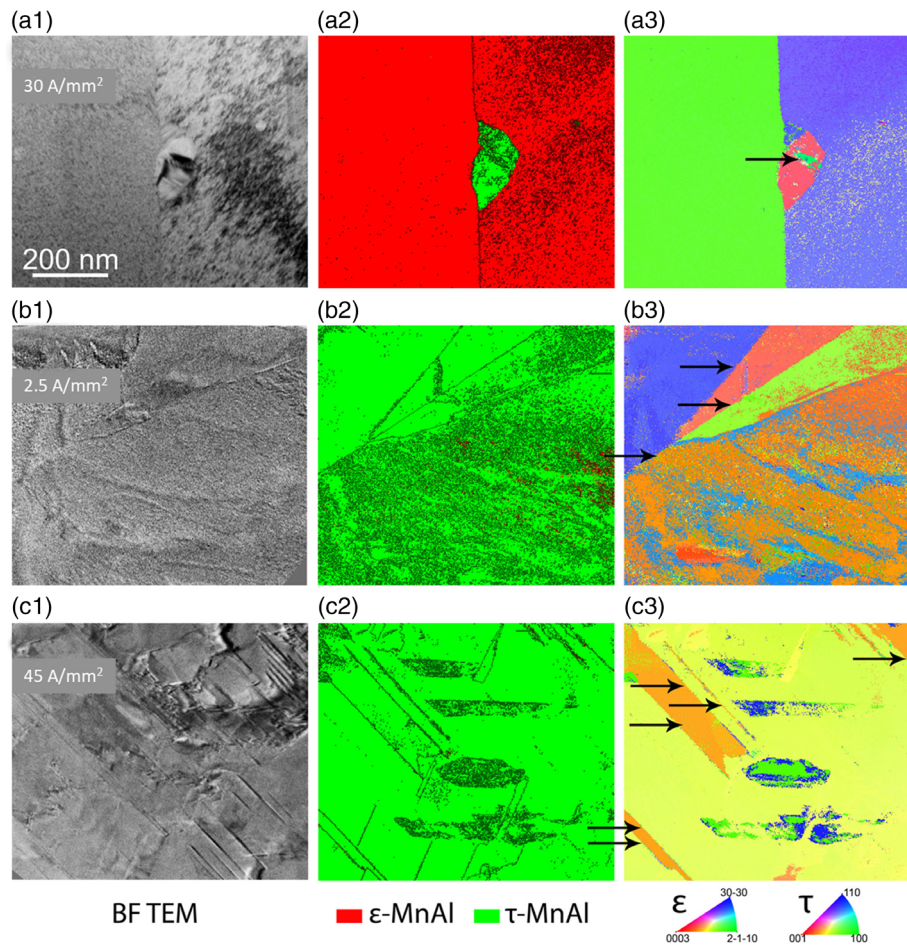


Figure 7. Transmission electron microscope (TEM) analysis on the partially transformed sample a) showing a1) bright-field (BF) TEM image, a2) automated crystal orientation mapping (ACOM) phase map indicating the τ -phase nucleation, and a3) ACOM inverse-pole figure (IPF) map indicating that the τ -phase grain originates at the grain boundary of the ϵ -phase. b,c) Fully transformed samples under lowest and highest electric current density, 2.5 and 45 A mm⁻², respectively, are shown in BF TEM and ACOM phase and orientation mappings as in (a). Arrows mark true twin boundaries with a 76° misorientation angle.

Figure 7a1 shows the bright-field (BF) TEM image of the partially transformed sample, in combination with the automated crystal orientation mapping (ACOM) showing the phase map (Figure 7a2) and the corresponding inverse-pole figure (IPF, Figure 7a3). One notices that the τ -phase is nucleating at the grain boundary of the parent ϵ -phase grains. The grain boundaries have been reported to be the preferential site for heterogeneous nucleation of the metastable τ -phase.^[25,38] However, in the context of this work, this preferential site can also be related to the “hot spots,” since grain boundaries have a different atomic arrangement and contain a high density of defects, therefore it is expected that the electrical resistance is higher, leading to a local increase in temperature when subjected to a electric current flow.^[39,40]

Moreover, the IPF analysis reveals that the τ -phase nanometer-sized grain has an orientation along (001) direction, showing also a twinned region with orientation close to (100), as indicated by the arrow in Figure 7a3. The misorientation across the twin variants is around 76°, corresponding to “true twin”-type

boundary.^[17,36,41] This typical twin configuration in the τ -phase of Mn–Al-based alloys has been reported to be the one with the highest frequency in comparison with the other two types of possible twins, that is, pseudo twin (misorientation of 48°) and order twin (misorientation of 85°).^[17]

Similarly, the fully transformed samples, as confirmed by the phase map analysis (Figure 7b2,c2), under different electric current densities also show true twin boundaries, highlighted by the arrows in Figure 7b3,c3, pseudo and order twins were not observed. In more detail, **Figure 8** shows the selected area diffraction pattern (SAED, Figure 8a) of the corresponding dark-field (DF) TEM image (Figure 8b) of the sample annealed under 45 A mm⁻². The diffraction pattern confirms the presence of twins as two mirrored patterns are observed for the and [-101] orientations. Simulated diffraction spots are marked in orange and purple. Double diffraction is observed causing additional diffraction spots.^[42] Streaks along the (111) axis, marked by arrows, indicate the formation of stacking faults.^[17] The composite-centered DF TEM image (Figure 8b) of the

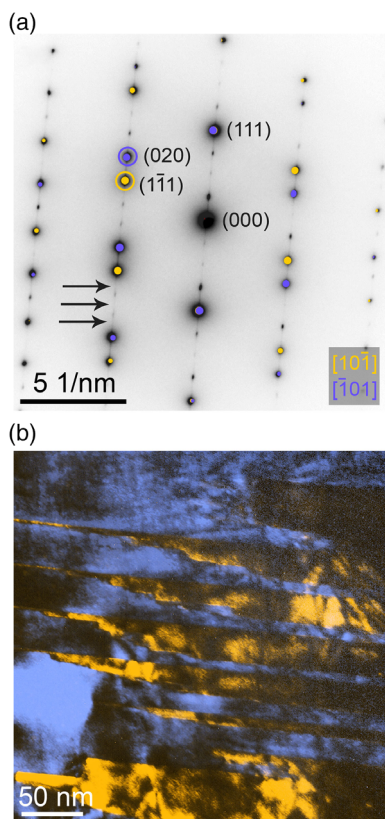


Figure 8. Selected area electron diffraction (SAED) pattern of a) the region containing twins depicted in the colored dark-field (DF) image of b) the sample annealed under 45 A mm^{-2} . The composite-centered DF TEM image (b) is related to the selected diffraction spots marked with circles in (a) with matching color codes.

selected diffraction spots marked with circles in Figure 8a. For each twin orientation, a corresponding diffraction spot was selected, (1-11) for and (020) for $[-101]$ respectively, and the images were combined in color coded accordingly. Distinctly, “saw tooth/jagged edge” shaped twins with varying sizes of below 10 nm are observed in the region of interest, in contrast to the hundred-nanometer sized observed in Figure 7.

The samples show similar microstructural features upon phase transformation, independently from the τ -phase fraction or the electric current density used during annealing, despite the macroscopic temperature difference for the onset transformation. These features are comparable to the ones reported in literature for different annealing procedures and processes, including field-assisted techniques such as SPS.^[17,25] It is known that the twins, and the associated stacking faults, in this material system are formed during the shearing mechanism of the ϵ -phase to τ -phase transformation and have an impact on the magnetic properties, more specifically on the coercivity. These twin boundaries act as nucleation centers for reversal domains, meaning that it limits and creates a threshold of the coercivity values, 0.12–0.14 T in our study, as observed previously on the hysteresis loops in the partially and fully transformed samples (Figure 3 and 6).

3. Conclusion

We investigated the effect of electric current-assisted annealing on the formation of the ferromagnetic metastable τ -phase in Mn–Al–C compound using an in-house-built specific purpose device. It was found that the $\epsilon \rightarrow \tau$ onset transformation can be shifted to lower temperatures upon increasing the DC electric current density during annealing, reaching a maximum shift of 140 °C observed in our study. This significant difference can be used to avoid the decomposition of the metastable τ -phase, preserving the hard magnetic properties in contrast to detriment caused by the appearance of the nonmagnetic stable phases in this material system. Moreover, the use of in situ electrical resistance measurements in our experimental setup have shown to accurately probe the phase transition, as given by the lower electrical resistivity of the ferromagnetic phase in comparison to the parent ϵ -phase. The correlation between phase formation and electrical resistance can be further used to engineer microstructures and phases, which can be potentially used for other compounds including metastable ones as the demonstrated in our case.

Microstructural TEM-based analysis revealed that grain boundaries are nucleation centers for the emerging ferromagnetic phase. This finding can be correlated to the creation of hot spots related to the electric current-assisted annealing process and also to the preferential site for heterogeneous nucleation at this defect. Upon phase transformation, the appearance of true twin boundaries were observed, even at early stage of the τ -phase nucleation and growth. The resulting microstructure of pure ferromagnetic phase samples containing true twin boundaries, and associated stacking faults, explains the obtained high magnetization and the similar coercivity values, respectively. Both microstructure and magnetic properties of the samples were similar, being independent from the electric current density used during annealing and comparable to other methods reported in literature, showing that using electric current can be applied to change the onset temperature of phase transformation and still preserve the functional magnetic properties.

4. Experimental Section

Experimental Setup: An in-house built experimental setup was developed to study the influence of electric current-assisted annealing, in direct current mode (DC), on the phase-transition behavior of Mn–Al–C material system. The setup consisted of an insert (sample holder), power supply (current generator), and measurements electronics. Additional external heat source (oven) was used with a fixed heating rate of 5 K min^{-1} in all experiments. Simultaneous measurement of the electric resistance and temperature of the sample were used to control and monitor the solid-state phase transition during current-assisted heat treatment. Two S-type thermocouples were used to measure in situ the macroscopic temperature of the sample, while the electrical resistance of the sample was calculated by measuring the voltage difference between the platinum wires of both thermocouples. Three digital multimeters were used to record the signal of electric current, resistance, and temperature. Reliable contact between the sample with the electrical contacts and thermocouples during the thermal treatment were ensured using a system with clamping levers and springs. More detailed information about the experimental setup can be found in Ref. [27].

Sample Preparation and Characterization: The initial bulk ingot of $\text{Mn}_{5.4}\text{Al}_{4.4}\text{C}_2$ alloy was prepared by induction melting of high-purity elements (purity above 99.8%) under protective argon gas atmosphere.

Extra 3 wt% of Mn was added to compensate evaporation losses. Subsequently, the ingot was subjected to melt spinning (Bühler Melt-Spinner SC) by ejecting the molten alloy through a nozzle (0.5 mm) onto a copper wheel with tangential velocity of 20 m s^{-1} to produce ribbons. The melt-spun ribbons were used to study the phase transition between the high-temperature ϵ -phase, obtained due to the fast quenching rate during melt spinning, and the metastable ferromagnetic τ -phase during electrical current-assisted annealing. The DC electric current density was varied to evaluate the effect of this parameter during the annealing.

DSC (Netzsch 404 F1 Pegasus) was used to identify the phase-transition temperature of $\text{Mn}_{54}\text{Al}_{44}\text{C}_2$ in the as-spun state. The heating rate was kept the same as in the electric current-assisted annealing, that is, 5 K min^{-1} , from room temperature up to $550 \text{ }^\circ\text{C}$, under protective atmosphere using a mixture of nitrogen and helium gas flow. Aluminum crucibles were chosen for this analysis.

The crystal structure was characterized by XRD. The measurements were carried out on a Stoe Stadi P diffractometer with $\text{Mo K}\alpha_1$ radiation, in transmission mode, and with an angular 2θ range from 5° to 50° . Phase matching and phase fraction were calculated from Rietveld refinement using FullProf/WinPLOT suite software.^[43,44]

Isothermal magnetization measurements were performed on the ribbons before and after annealing using physical property measurement system-vibrating sample magnetometer (PPMS-VSM) (Quantum Design PPMS-14), at room temperature, under applied magnetic field up to 3 T.

The microstructure was investigated using TEM. The electron-transparent lamellae were prepared using focused-ion beam (FIB) instrument (Thermo-Scientific Helios G4 Dual Beam System) with an in situ, in-plane-lift-out standard procedure. BF and DF TEM imaging, selected area electron diffraction, as well as scanning precession electron diffraction (SPED) were performed on a JEOL JEM-ARM200F, operated at 200 kV, equipped with a direct electron detector (Quantum Detectors, Merlin EM). For SPED, a probe convergence of 5 mrad was used, and pixel pitch was selected as 1.75 nm. Data analysis was performed with the ASTAR software package (NanoMEGAS SPRL).

Acknowledgements

This work was funded by the Deutsche Forschungsgemeinschaft (DFG, German Research Foundation) within the framework of the Priority Programme SPP1959 Fields Matter. This work was supported by the European Research Council (ERC) "Horizon 2020" Program under Grant No. 805359-FOXON and Grant no. 957521-STARE. The authors acknowledge the assistance of Dr. Stefan Riegg on the DSC analysis and Volker Radisch for the FIB preparation.

Open Access funding enabled and organized by Projekt DEAL.

Conflict of Interest

The authors declare no conflict of interest.

Data Availability Statement

The data that support the findings of this study are available from the corresponding author upon reasonable request.

Keywords

electric current-assisted annealing, metastable phase, Mn–Al–C permanent magnets, phase transformation

Received: December 13, 2022
Published online: February 15, 2023

- [1] J. Cui, M. Kramer, L. Zhou, F. Liu, A. Gabay, G. Hadjipanayis, B. Balasubramanian, D. Sellmyer, *Acta Mater.* **2018**, *158*, 118.
- [2] J. M. D. Coey, *Scr. Mater.* **2012**, *67*, 524.
- [3] P. Zhao, L. Feng, K. Nielsch, T. G. Woodcock, *J. Alloys Compd.* **2021**, *852*, 156998.
- [4] K. P. Skokov, O. Gutfleisch, *Scr. Mater.* **2018**, *154*, 289.
- [5] L. Pareti, F. Bolzoni, F. Leccabue, A. E. Ermakov, *J. Appl. Phys.* **1986**, *59*, 3824.
- [6] A. Trench, J. P. Sykes, *Engineering* **2020**, *6*, 115.
- [7] K.-H. Müller, S. Sawatzki, R. Gauß, O. Gutfleisch, in *Handbook Of Magnetism And Magnetic Materials*, Springer International Publishing, Berlin, Germany **2021**, pp. 1–65.
- [8] M. D. Kuz'min, K. P. Skokov, H. Jian, I. Radulov, O. Gutfleisch, *J. Phys.: Condens. Matter* **2014**, *26*, 064205.
- [9] L. Feng, J. Freudenberger, T. Mix, K. Nielsch, T. G. Woodcock, *Acta Mater.* **2020**, *199*, 155.
- [10] R. W. McCallum, L. Lewis, R. Skomski, M. J. Kramer, I. E. Anderson, *Annu. Rev. Mater. Res.* **2014**, *44*, 451.
- [11] F. Bittner, L. Schultz, T. G. Woodcock, *J. Alloys Compd.* **2017**, *727*, 1095.
- [12] D. Palanisamy, D. Raabe, B. Gault, *Acta Mater.* **2019**, *174*, 227.
- [13] Y. Jia, Y. Wu, S. Zhao, J. Wang, C. Jiang, *Intermetallics* **2018**, *96*, 41.
- [14] R. Madugundo, O. Koylu-Alkan, G. C. Hadjipanayis, *AIP Adv.* **2016**, *6*, 056009.
- [15] P.-Z. Si, H.-D. Qian, C.-J. Choi, J. Park, S. Han, H.-L. Ge, K. Shinde, *Materials* **2017**, *10*, 1016.
- [16] C. Zhang, T. Zhang, J. Wang, S. Zhao, Y. Wu, C. Jiang, *Scr. Mater.* **2018**, *143*, 72.
- [17] Y. Jia, H. Ding, Y. Wu, J. Wang, H. Wu, T. Ma, S. Zhao, K. P. Skokov, A. Aubert, F. Maccari, O. Gutfleisch, Y. Xu, J. Niu, B. Qiao, S. Zhao, C. Jiang, *Acta Mater.* **2022**, *232*, 117892.
- [18] S. Zhao, Y. Wu, C. Zhang, J. Wang, Z. Fu, R. Zhang, C. Jiang, *J. Alloys Compd.* **2018**, *755*, 257.
- [19] O. Guillon, C. Elsässer, O. Gutfleisch, J. Janek, S. Korte-Kerzel, D. Raabe, C. A. Volkert, *Mater. Today* **2018**, *21*, 527.
- [20] S. Ener, K. P. Skokov, D. Y. Karpenkov, M. D. Kuz'min, O. Gutfleisch, *J. Magn. Magn. Mater.* **2015**, *382*, 265.
- [21] D. E. Laughlin, *Metall. Mater. Trans. A* **2019**, *50*, 2555.
- [22] S. Rivoirard, *JOM* **2013**, *65*, 901.
- [23] H. Conrad, *Mater. Sci. Eng. A* **2000**, *287*, 227.
- [24] R. Kobayashi, Y. Mitsui, R. Y. Umetsu, K. Takahashi, M. Mizuguchi, K. Koyama, *Mater. Trans.* **2017**, *58*, 1511.
- [25] F. Maccari, A. Aubert, S. Ener, E. Bruder, I. Radulov, K. Skokov, O. Gutfleisch, *J. Mater. Sci.* **2022**, *57*, 6056.
- [26] Z. H. Lai, H. Conrad, G. Q. Teng, Y. S. Chao, *Mater. Sci. Eng. A* **2000**, *287*, 238.
- [27] F. Maccari, D. Y. Karpenkov, E. Semenova, A. Y. Karpenkov, I. A. Radulov, K. P. Skokov, O. Gutfleisch, *J. Alloys Compd.* **2020**, *836*, 155338.
- [28] A. D. Crisan, A. Leca, C. Bartha, I. Dan, O. Crisan, *Nanomaterials* **2021**, *11*, 896.
- [29] V. Rao, A. Mitra, *J. Therm. Anal. Calorim.* **1995**, *44*, 375.
- [30] P. Allia, M. Barricco, M. Knobel, P. Tiberto, F. Vinai, *J. Magn. Magn. Mater.* **1994**, *133*, 243.
- [31] S. Kim, M. Choi, H. Won, H.-S. Lee, W. Lee, S.-G. Kim, W. Lee, Y.-K. Hong, *J. Alloys Compd.* **2022**, *919*, 165773.
- [32] T. Keller, I. Baker, *Progr. Mater. Sci.* **2022**, *124*, 100872.
- [33] Y. Jia, Y. Wu, S. Zhao, S. Zuo, K. P. Skokov, O. Gutfleisch, C. Jiang, H. Xu, *Phys. Rev. Mater.* **2020**, *4*, 094402.

- [34] V. V. Popov, F. Maccari, I. A. Radulov, A. Kovalevsky, A. Katz-Demyanetz, M. Bamberger, *Manuf. Rev.* **2021**, *8*, 10.
- [35] D. Palanisamy, A. Kovács, O. Hegde, R. E. Dunin-Borkowski, D. Raabe, T. Hickel, B. Gault, *Phys. Rev. Mater.* **2021**, *5*, 064403.
- [36] S. Bance, F. Bittner, T. G. Woodcock, L. Schultz, T. Schrefl, *Acta Mater.* **2017**, *131*, 48.
- [37] F. Bittner, J. Freudenberger, L. Schultz, T. G. Woodcock, *J. Alloys Compd.* **2017**, *704*, 528.
- [38] J. M. K. Wiezorek, A. K. Kulovits, C. Yanar, W. A. Soffa, *Metall. Mater. Trans. A* **2010**, *42*, 594.
- [39] H. Bishara, M. Ghidelli, G. Dehm, *ACS Appl. Electron. Mater.* **2020**, *2*, 2049.
- [40] H. Bishara, S. Lee, T. Brink, M. Ghidelli, G. Dehm, *ACS Nano* **2021**, *15*, 16607.
- [41] M. Gusenbauer, A. Kovacs, H. Oezelt, J. Fischbacher, P. Zhao, T. G. Woodcock, T. Schrefl, *J. Appl. Phys.* **2021**, *129*, 093902.
- [42] C. Cayron, *Scr. Mater.* **2021**, *194*, 113629.
- [43] J. Rodríguez-Carvajal, *Phys. B Condens. Matter* **1993**, *192*, 55.
- [44] T. Roisnel, J. Rodríguez-Carvajal, *Mater. Sci. Forum* **2001**, *378–381*, 118.